Damping Behavior in a Wide Temperature Range of FeMn-Like High Entropy Shape Memory Alloys

L. Peltier[1] · P. Lohmuller[2] · F. Meraghni[1] · E. Patoor[3] · P. Laheurte[2] · S. Berveiller[1]

Abstract In this work, a new class of iron-based high entropy shape memory alloys (HE-SMAs) have been designed, characterized, and optimized. These FeCuNiMnV alloys (FeMn-like) with damping properties at low and high temperatures are developed; a methodology is proposed to demonstrate how to preserve this effect from the memory loss observed on conventional damping alloys. The developed alloys are analyzed using X-ray diffraction, scanning electron microscopy and differential scanning calorimetry. Their damping capacity is investigated using a drop weight test device instrumented with a digital image correlation system for the displacement measurement. It is compared with one of FeMnV, NiTi, CuAlNi, and 1050A alloys at different temperatures. The results show that the damping capacity is interesting over a wide range of operating temperatures. It has been established that the cocktail effect obtained by mixing Cu, Fe, Ni, Mn, and V elements allows for optimizing the damping capacity of the HE-SMAs. In addition, the sluggish diffusion may allow these HE-SMAs to prevent the premature aging that leads to a degradation of the damping behavior notably at high temperature. The variation of the composition of the Cu_x-$Fe_yNi_zMn_{20}V_{11}$ alloys enables the adjustment of the alloying element content by favoring the appearance of the non-thermally activated martensite keeping hence a stable damping behavior from − 40 to 200 °C.

Keywords High entropy alloys · Shape memory alloys · Damping behavior · Martensitic transformation · Cold forming

This invited article is part of a special issue of *Shape Memory and Superelasticity* honoring Etienne Patoor for his contributions to the field of phase transforming materials and shape memory alloys. The special issue was organized by Dr. Fodil Meraghni, Ecole Nationale Supérieure d'Arts et Métiers (Arts et Métiers Institute of Technology), and Dr. Dimitris Lagoudas, Texas A&M University.

✉ L. Peltier
laurent.peltier@ensam.eu

[1] LEM3, Arts et Métiers Institute of Technology, Université de Lorraine, CNRS, HESAM Université, 4, rue Augustin Fresnel, 57070 Metz, France

[2] LEM3, Université de Lorraine, Arts et Métiers Institute of Technology, CNRS, 7, rue Félix Savart, 57070 Metz, France

[3] GT-UMI 2958 Georgia Tech-Lorraine, CNRS, 2 rue Marconi, 57070 Metz, France

Introduction

Research on high entropy alloys (HEAs) is extensively conducted during the last decade due to the high mechanical potential of this new class of alloys [1]. HEAs are generally defined as alloys containing at least five elements, with equimolar or near equimolar compositions [2]. The advantages of high entropy are high hardness level, high strength when used at elevated temperatures and a sensitive increase of corrosion and wear resistance [3]. Moreover, HEAs generally form a simple solid solution (FCC or BCC) at the detriment of the formation of intermetallic phases [4]. The element composition of the alloy is an important factor affecting its behavior and performance [5].

Fe-based and Cu-based shape memory alloys are very good candidates for civil applications requiring damping capabilities [6, 7]. Several families of SMAs are known for their damping effect: MnCu-type alloys [8–10], FeMn-type alloys [11–16], NiMn-type alloys [17, 18], NiTi-type alloys [19], CuAl-type alloys [20], and TiNb-type alloys [21]. Some of these families have known deficiencies such as

loss of memory effect (or amnesia) for MnCu and CuAl [22–24] type alloys or too much temperature dependency for NiTi and CuAl-type alloys [25–28]. Jensen et al. [29] even show a significant loss of the damping effect of the binary MnCu alloy during long and unstressed storage. These features are unsuitable for industrial applications and their related reliability. The quaternary alloys M2052 (MnNiCuFe) [30–32] and SONOSTRON (MnCuFeAl) [33] known for their damping effect already appear as the mixing of several families of SMAs but are also subject to the degradation of the damping capacity observed during their storage [34]. Some recent studies already show the possibility of producing quinary alloys with a damping behavior whose entropy is high but does not correspond to the high entropy criterion [14, 35–38]. Other studies are investigating the behavior of HEAs with damping characters doped with oxygen and nitrogen [39].

This study aims at producing new high entropy shape memory FeMn-like alloys (HE-SMA) derived from the ternary $Fe_{67}Mn_{22}Cr_{11}$ alloy developed by Okada et al. [40]. The damping capabilities shall be valid over a wide temperature range (− 40 to 200 °C) and the microstructure shall allow a high ductility and improved cold formability.

The novelty of this paper resides in the methodology enabling to sum up the effects related to the high entropy to build a new type of FeMn-like damping alloys. The pseudoelastic effect, which is very low subject to temperature is generated by the as-cast structure of the alloy and the optimized internal compressive stresses due to the crystal lattice distortion. On the other hand, to the best of the authors' knowledge, there has been no comparative work on the simultaneous effects of high entropy on the manufacturing formability and the aging of shape memory damping alloys.

This paper is organized as follows: in section "Choosing the Chemical Composition of the Studied Alloys", the choice of the five elements constituting the studied HEAs and the weighting of these five elements is presented and detailed using the equivalence parameters and the criteria related to the metallurgy of the HEAs allowing to transform a low entropy SMA into a high entropy SMA (HE-SMA). Section "Experimental Procedure" is devoted to the melting, heat treatment processing, and the test bench to evaluate damping properties. In section "Experimental Results", the results of the different tests are presented, depending on the test temperature and the metallurgical state of the alloys. Test results of the four HE-SMAs produced for this work are then compared with those of a ternary alloy from which these HE-SMAs are derived, as well as to those of a NiTi alloy and a ternary CuAlNi alloy.

Choosing the Chemical Composition of the Studied Alloys

Presentation of Equivalent Elements for the Transformation of a Ternary Alloy into a Quinary Alloy

Figure 1 shows the equivalent elements for the six main chemical elements that can constitute alloys with damping properties. In the case of the ternary FeMnCr alloy, Fe can be partially replaced by Co, Ni, and Cu in period 4, Pd in period 5, Pt and Au in period 6. The element Cr can be partially replaced by V in period 4, Mo in period 5, and W in period 6. The element Mn has no other equivalent.

In the design of a new damping alloy that can be used over a wide temperature range, some element pairs such as Ti–Ni and Cu–Al must naturally be avoided to limit the appearance of the thermal memory effect. This temperature dependency of the damping effect is highlighted by the studies of Piedboeuf et al. [25], He et al. [26], Yin et al. [27], and Toker et al. [28] in the titanium and copper-based SMAs. On the other hand, FeNi-X SMAs (where X is Cu, Cr, Mn, Mo) are known to exhibit a non-thermal martensitic phase transformation [40–42].

Presentation of the HEA Criteria

According to the work by Zhou et al. [2], the high entropy of an alloy is only operative if the mixing entropy value, ΔS_{mix}, is greater than $1.5R$, where R is the gas constant ($R = 8.314$ J K^{-1} mol^{-1}). In addition, Zhou et al. also show the content of different elements is between 5 and 35 at.%. Several criteria are used in high entropy alloy metallurgy to increase the predictability of the single-phase solid solution formation. These criteria are based on the work of Hume-Rothery [43]. The first criterion is the term ΔH_{mix}, which represents the average of the binary mixing enthalpies obtained between each of the pairs of elements in the alloy. An enthalpy close to zero or negative in the Gibbs equation stabilizes the formation of solid solutions. The second criterion concerns the difference in atomic radius for each element constituting the alloy. It should be noted that the integration of the different atoms in the HEA crystalline lattice is easier when the difference between the atomic radii (R_a) is the smallest. Thus, the solubility of the different elements is increased because the distortion of the crystalline lattice is reduced. The third criterion is the difference in Pauling electronegativity between the "n" elements of the alloy. The fourth criterion is the average valence electron concentration (VEC). The third and fourth criteria are used to predict the type of crystallographic structure generated by the development of a high entropy

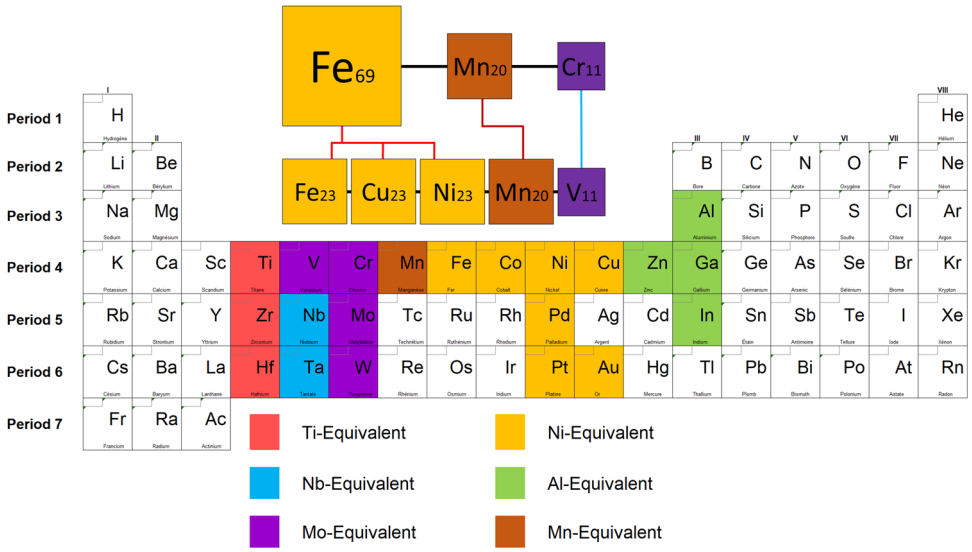

Fig. 1 Periodic elements table showing the different equivalent elements for those commonly used in damping alloys composition

alloy [44–46]. Based on the work of Cantor et al. [1], the elements of transformation of the ternary alloy into a quinary alloy must all belong to the same period. In our case, only elements from period 4 fit this requirement and were considered in the following to define the composition of the designed alloys. Hence, the different criteria established for obtaining a HEA [4, 44, 46], such as enthalpy, atomic radius difference, the difference of electronegativity between all the constitutive elements and the average of the valence electrons (VEC) are optimized.

Multi-criteria Validation of the Alloy Compositions

The enthalpy criterion is determined based on the enthalpy of all the element pairs contained in the quinary alloy. As illustrated in Table 1, element pairs of period 4 (Ti–Ni, Ti–Fe, Ti–Co, Ti–Zn, V–Co, V–Ni, Cu–Cr, Cu–Fe) have to be avoided since their combination enthalpy value is not ranging between − 10 and 10 kJ mol^{-1}.

From the criteria, the chemical equivalent composition was set as $Cu_xFe_yNi_zMn_{20}V_{11}$; the pseudo-ternary graph $Cu_xFe_yNi_zMn_{20}V_{11}$ shown in Fig. 2 highlights the five chosen alloys. In the remainder of the present paper, the alloys will be named as follows:

- $A_{0–69}$ for the ternary $Fe_{69}Mn_{20}V_{11}$ alloy,
- $A_{23–23}$ for the quinary $Cu_{23}Fe_{23}Ni_{23}Mn_{20}V_{11}$ alloy,
- $A_{29–11}$ for the quinary $Cu_{29}Fe_{11}Ni_{29}Mn_{20}V_{11}$ alloy,
- $A_{29–29}$ for the quinary $Cu_{29}Fe_{29}Ni_{11}Mn_{20}V_{11}$ alloy, and
- $A_{11–29}$ for the quinary $Cu_{11}Fe_{29}Ni_{29}Mn_{20}V_{11}$ alloy.

Table 2 compares the parameters considered for high entropy for damping HEA of the literature. The CrMnFeCoNi alloy studied by Cantor et al. [1] perfectly fits the different criteria for obtaining a single solid solution. It is worth mentioning that only the four high entropy alloys proposed in this study meet the five selected criteria unlike the other four alloys in the literature [14, 35–38].

Experimental Procedure

Manufacturing Stages and Heat Treatments

The five alloys $A_{0–69}$ to $A_{11–29}$ were produced using raw materials with a purity greater than 99.9 wt% provided by

Table 1 Chemical mixing enthalpies (kJ mol^{-1}) for atomic pairs among them the alloying elements of the fourth period of the periodic table of elements

	Ti	V	Cr	Mn	Fe	Co	Ni	Cu	Zn
Ti		-2	-7	-8	-17	-28	-35	-9	-15
V	-2		-2	-1	-7	-14	-18	5	-2
Cr	-7	-2		2	-1	-4	-7	12	5
Mn	-8	-1	2		0	-5	-8	4	-6
Fe	-17	-7	-1	0		-1	-2	13	4
Co	-28	-14	-4	-5	-1		0	6	-5
Ni	-35	-18	-7	-8	-2	0		4	-9
Cu	-9	5	12	4	13	6	4		1
Zn	-15	-2	5	-6	4	-5	-9	1	

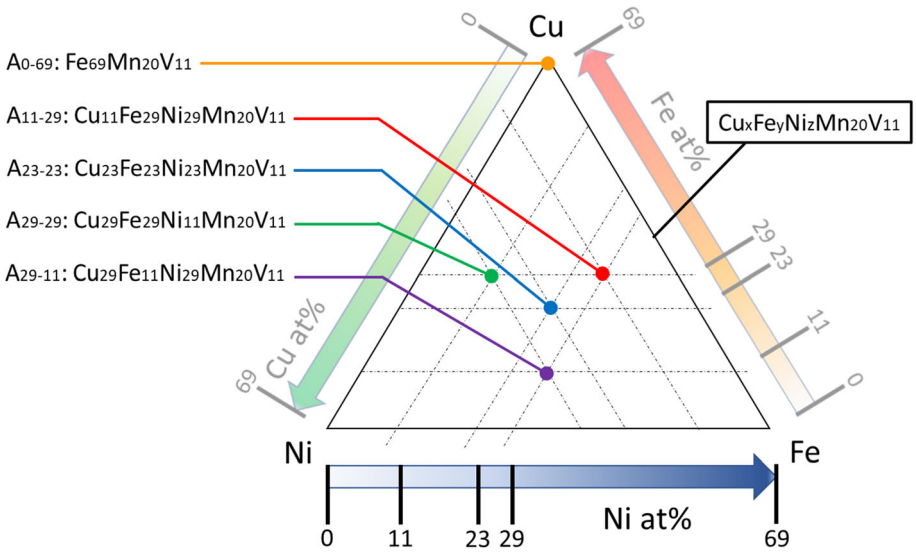

Fig. 2 $Cu_xFe_yNi_zMn_{20}V_{11}$ pseudo-ternary diagram

Table 2 Criteria for microstructures formation, ΔS_{mix} and ΔH_{mix} correspond to mixing entropy and enthalpy, respectively, δ corresponds to the relative radii difference, EN means electronegativity, whereas VEC stands for valence electron concentration

Alloys			ΔSmix (J/K/mol) x>1.5	ΔHmix (kJ/mol) xϵ[-10;10]	δ (%) xϵ[0;6.6]	EN Pauling x≈0	VEC x≠[6.87;7.99]
CrMnFeCoNi	Cantor et al.	[1]	1.61 ☑	-4.16 ☑	3.27 ☑	0.14 ☑	8.00 ☑
$Fe_{69}Mn_{20}V_{11}$	Present work	$A_{0\text{-}69}$	0.82 ☒	-2.21 ☑	3.60 ☑	0.12 ☑	7.47 ☒
$Cu_{23}Fe_{23}Ni_{23}Mn_{20}V_{11}$	Present work	$A_{23\text{-}23}$	1.58 ☑	0.33 ☑	3.26 ☑	0.14 ☑	8.62 ☑
$Cu_{29}Fe_{11}Ni_{29}Mn_{20}V_{11}$	Present work	$A_{11\text{-}29}$	1.52 ☑	-0.26 ☑	3.13 ☑	0.15 ☑	8.92 ☑
$Cu_{29}Fe_{29}Ni_{11}Mn_{20}V_{11}$	Present work	$A_{29\text{-}29}$	1.52 ☑	3.64 ☑	3.20 ☑	0.14 ☑	8.56 ☑
$Cu_{11}Fe_{29}Ni_{29}Mn_{20}V_{11}$	Present work	$A_{29\text{-}11}$	1.52 ☑	-3.04 ☑	3.40 ☑	0.14 ☑	8.38 ☑
$Fe_{50}Mn_{20}Co_{15}Cr_{15}$	Wang et al.	[14]	1.23 ☒	-1.32 ☑	3.35 ☑	0.12 ☑	7.65 ☒
$Al_{0.25}CoCrFeNi$	Ma et al.	[35]	1.53 ☑	-6.75 ☑	3.49 ☑	0.11 ☑	7.93 ☒
$CrMn_{0.5}FeVCu_{0.1}$	Song et al.	[36]	1.44 ☒	-1.94 ☑	3.25 ☑	0.10 ☑	6.56 ☑
$Fe_{85.4}Cr_{11}Mo_{2.5}Zr_{0.1}Ni_1$	Chen K. et al.	[37]	0.52 ☒	-0.74 ☑	1.78 ☑	0.08 ☑	7.74 ☒
$Fe_{60}Mn_{20}Co_5Cr_{15}$	Chen Q. et al.	[38]	1.06 ☒	-0.56 ☑	3.39 ☑	0.12 ☑	7.55 ☒

☒ Criterion not validated
☑ Criterion validated

Goodfellow company. The alloys were elaborated in a cold crucible, equipped with a pyrometer that measures the melting temperature (T_m) of the alloy. Before heating, the protective atmosphere of the furnace was flushed five times with ultra-pure Argon and a vacuum pump. Melting was performed with a pressure of 900 mBar of ultra-pure Argon. Five melting cycles were performed to ensure the homogeneity of the different alloys. The ingots were then cast in a cylindrical mold of 16 mm diameter and 30 mm height. Three metallurgical states were considered for further characterization: the as-cast state (AC) corresponds to the state just after melting, the ST state is after solution heat treatment (900 °C 30 min) followed by severe water quenching, and a cold-worked state (CW) was obtained by cold rolling. Three industrial alloys were also considered for damping tests: the 1050A aluminum alloy, the NiTi alloy, and the CuAlNi alloy were in an as-received state (AR state).

Damping Behavior Characterization

The drop weight test is commonly used to determine the hardness and/or the damping behavior of a material [47–51]. In the present work, a calibrated metal ball (bearing steel, diameter 5 mm) was falling in a transparent quartz tube (1 m long). The ball was hitting a cylindrical sample to test its damping behavior. The test bench (Fig. 3) consisted of a heavy treated steel base with a cylindrical socket. The cylindrical sample (diameter 10 mm) of the tested alloy was positioned into the socket before testing. A manual trigger was allowing releasing the ball to launch the

test (Fig. 3c). A mechanical blocker was stopping the ball before the second bounce, which prevented multiple impacts on the surface of the tested sample. During the entire test, a high-speed camera (Fig. 3b) recorded the ball's fall, the impact and the first rebound. The steel base and the sample could be heated or cooled to perform temperature rebound tests from − 40 to 200 °C (Fig. 3d).

The drop weight tests have been performed for different metallurgical states and temperatures of the samples. The rebound height and the dent size after impact were analyzed. The rebound height is directly linked to the damping capability of the alloy. The dent size provides information on the physical phenomena that allow the damping and the dissipation of energy during the impact. The dent diameter and its depth were measured using a profilometer (Tesa-Visio). The tests were repeated 20 times for each temperature to refine the statistics. After each drop, the cylinders were polished to remove the dent and the hardened zone due to the ball impact. Figure 4 shows the three phenomena related to the damping behavior of SMAs. If the tested cylinder is in a 100% martensitic metallurgical state (shape memory effect noted hereafter SME), then the energy absorbed during the impact will be coupled with a residual macroscopic strain of the martensite. If the tested cylinder is in a 100% austenitic metallurgical state (superelastic effect, noted SE) or a two-phase martensite/austenite metallurgical state (pseudoelastic effect or PE), then the energy absorbed during the impact will be combined with a reversible elastic strain of the austenite.

It is commonly admitted that the drop tests may induce experimental scattering in terms of impacted zone and its size. On the opposite, the microhardness tests have a good spatial resolution and activate the phase transformation uniformly in the center of the samples and the size of the micro-indentations allows an accurate study by SEM. Vickers microhardness tests were thus performed on an Indentec Zwick ZHV1 machine with a mass of 1 kg and a holding time of 10 s.

Metallurgical Characterization

Microstructure observations were performed using a scanning electron microscope (SEM). The crystallographic structure of phases was identified by X-ray diffraction (XRD) using Cu-Kα radiation at room temperature (an accelerating voltage of 40 kV and an intensity of 30 mA); cell parameters were also determined.

A differential scanning calorimeter (DSC) was used to determine the transformation temperatures: the thermal transformation from martensite to austenite during heating was characterized by an endothermic peak and transformation points A_s and A_f (for Austenite Start and Austenite Finish). The reverse transformation from austenite to martensite upon cooling phase was characterized by an exothermic peak and transformation points M_s and M_f (for Martensite Start and Martensite Finish). The area (enthalpy in J g^{-1}) and the spacing (hysteresis) of the transformation peaks were also determined. The transformation temperatures were obtained according to ASTM F2004-17 [52] (sample of 40 mg, cooling and heating rate of 10 °C min^{-1}) using a SETARAM DSC 131 calorimeter. Enthalpy changes (ΔH) were obtained using the SETSOFT software.

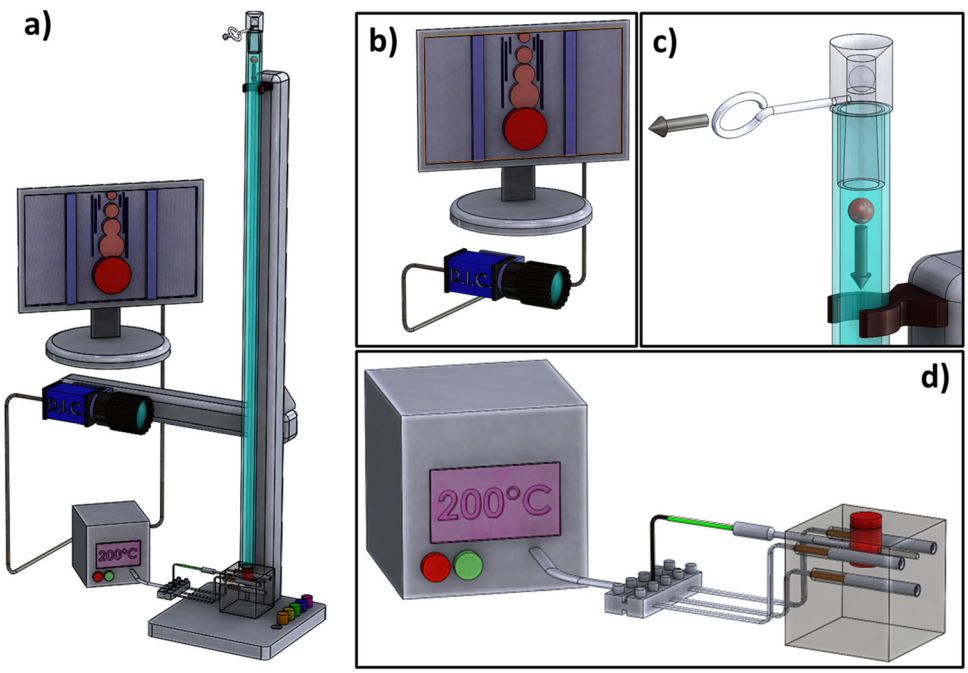

Fig. 3 An overview of the drop weight set-up: **a** General view of the drop column, **b** Monitoring of the DIC, **c** Manual trigger, **d** In red, cylindrical sample positioned in the instrumented heating steel base (color figure online)

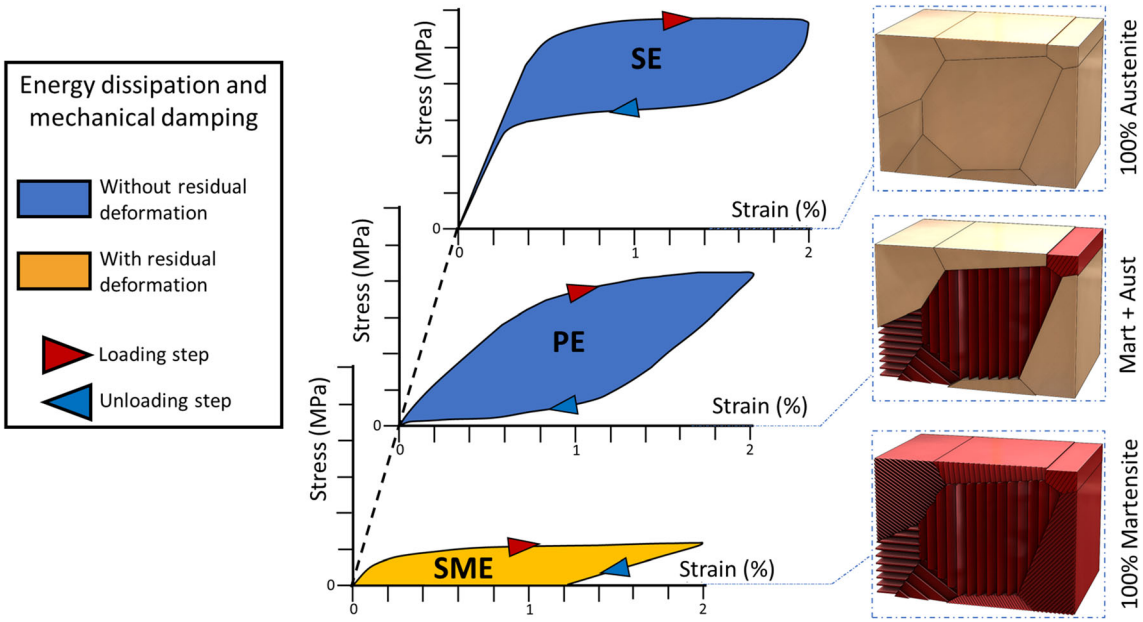

Fig. 4 Damping behavior of SMAs: superelasticity (SE) and pseudoelasticity (PE) are not coupled with residual strain, shape memory effect (SME) is coupled with residual strain

Experimental Results

Analysis of the Stress-Induced Phase Transformation at Room Temperature

First, drop weight tests were performed at room temperature on all the alloys considered in the ST state. XRD analysis was performed on the initial state and inside the dent after the impact (Fig. 5). Diffractograms have been indexed considering FCC or BCC structures. The ternary A_{0-69} alloy was mainly martensitic; weak peaks of austenite could be observed at the initial state but were not anymore present in the dent. The austenite cell parameter was equal to 0.353 nm. The A_{23-23} and A_{29-29} alloy diffractograms show two double peaks; they could have been indexed as two different austenite phases differing by their cell parameters, namely: a = 0.359 nm and a = 0.352 nm. No martensite was visible before nor after the impact as no peak was detected around 65°. The presence of two phases was confirmed by SEM observations (Fig. 6b, d): dendritic and globular structures were observed in the alloys. For the A_{29-11} alloy, diffraction peaks spread over a large 2θ-angle range, meaning that the two austenite phases were also present in this alloy; the SEM microstructure (Fig. 6c) shows a fine dendritic structure with two different phases. Only the A_{29-29} alloy was exhibiting one single-phase corresponding to the austenite with a cell parameter a = 0.352 nm; this was consistent with the SEM observation (Fig. 6). The cell parameter values are in agreement with the work of Yağcı et al. [53] on two ternary low entropy alloys: a martensitic FeMnV alloy with ΔS_{mix} = 0.54R and an austenitic FeMnCu alloy with ΔS_{mix} = 0.58R. They are also in agreement with the results of Choi et al. [54] who studied $V_{10}Cr_{10}Fe_{45}Co_{10}Ni_{35}$, a medium entropy alloy with ΔS_{mix} = 1.39R. This composition is close to the FeMnV-like one. Nevertheless, they had only one austenite phase (a = 0.359 nm).

As no martensite could be detected in the HE-SMAs after the drop test, Vickers indentation tests have been performed to determine if stress-induced martensite could be induced by one austenite or another.

Figure 6 shows SEM images of indentation. As can be seen, the indentation shows similar sizes whatever the alloy. The alloy's hardness was obtained by performing 10 Vickers tests; average values are reported in Table 3. The results of the hardness tests on NiTi, CuAlNi, and 1050A alloys were consistent with the literature [50, 55, 56]. The hardness of the ternary alloy A_{0-69} was similar to that of NiTi alloy and CuAlNi alloy (about 250 HV1). Except for the hardness of the 1050A alloy, one can claim that the A_{23-23} alloy has the lowest hardness (176 HV1) while the three other HE-SMAs have an equivalent hardness (around 185 HV1).

SEM observations reveal that the Vickers indentations in A_{0-69}, A_{23-23}, A_{29-11}, A_{29-29}, and A_{11-29} alloys (in the ST state) induce inelastic strain. Figure 7a shows the residual indentation with a mass of 1 kg. The size of the affected zone by this transformation varies according to the alloys and their microstructure. A mapping of this affected zone is shown in Fig. 7b.

The area where the inelastic deformation has occurred varies between the alloys. The smallest zone was observed

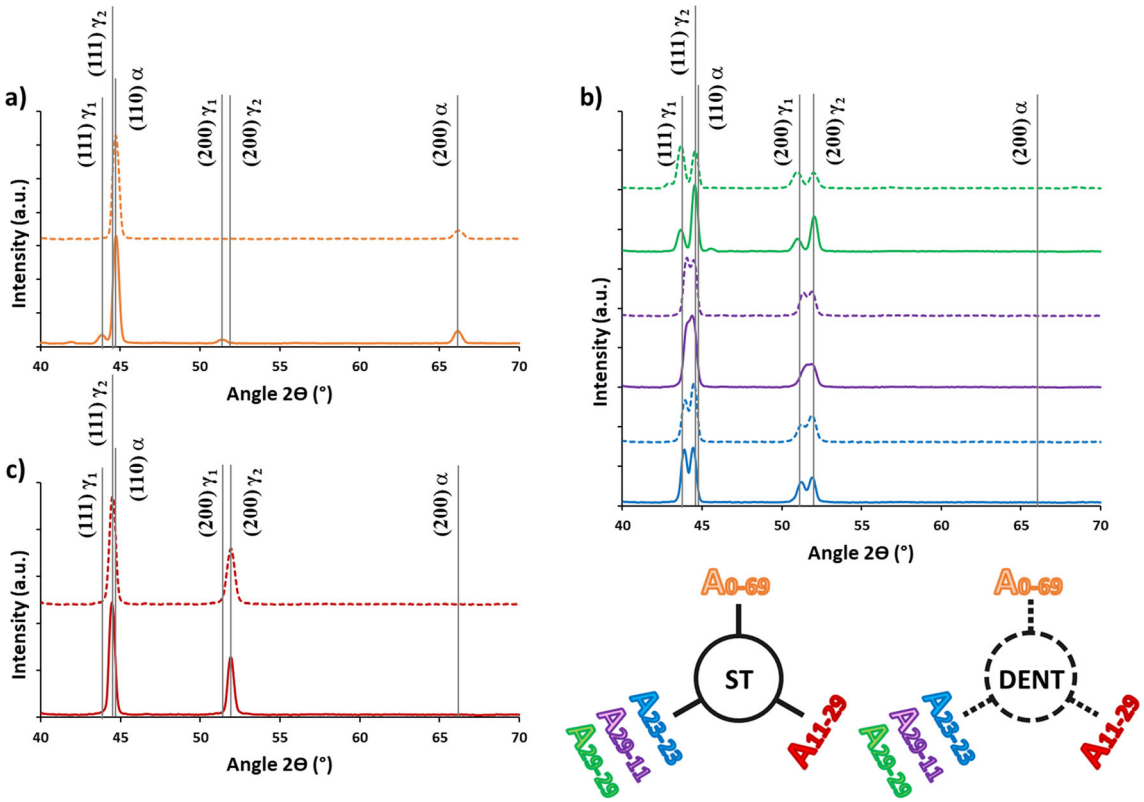

Fig. 5 Diffractograms of the alloys: **a** $A_{0–69}$ ternary alloy, **b** $A_{23–23}$, $A_{29–29}$ and $A_{29–11}$ quinary alloys and **c** $A_{11–29}$ quinary alloys. The diffractograms of the metallurgical states are differentiated: in solid lines are represented the diffractograms of the ST state and in dotted lines are the diffractograms inside the dent after the weight drop test

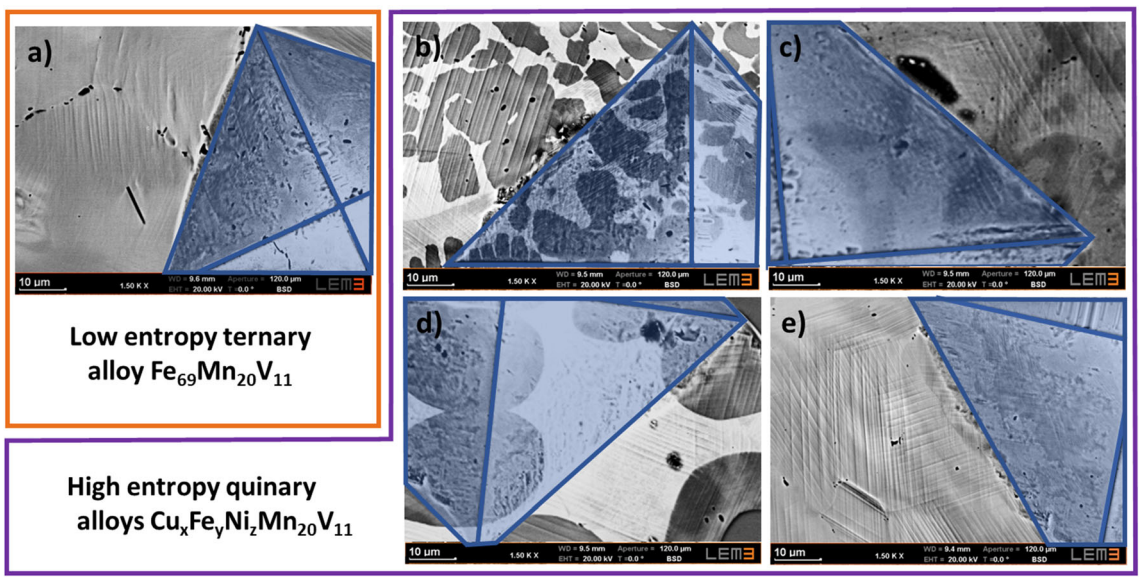

Fig. 6 SEM images of the edges of the indentations for the different alloys studied: **a** ternary single-phase $A_{0–69}$ alloy, **b** $A_{23–23}$, **c** $A_{29–11}$, **d** $A_{29–29}$, **e** single-phase quinary $A_{11–29}$ alloy. The indentation is represented in blue on the five thumbnails (color figure online)

in the ternary $A_{0–69}$ alloy which was martensitic. Inelastic strain by martensite reorientation is thus supposed to take place. The four quinary HE-SMAs were austenitic, so martensitic transformation was expected near the indentation. The most extended phase transformation was observed on the HE-SMA $A_{11–29}$; its initial microstructure

Table 3 Vickers hardness of the different samples studied

Alloys	1050A	NiTi	CuAlNi	A_{0-69}	A_{23-23}	A_{29-11}	A_{29-29}	A_{11-29}
Hardness HV1	37	231	215	253	176	192	189	185

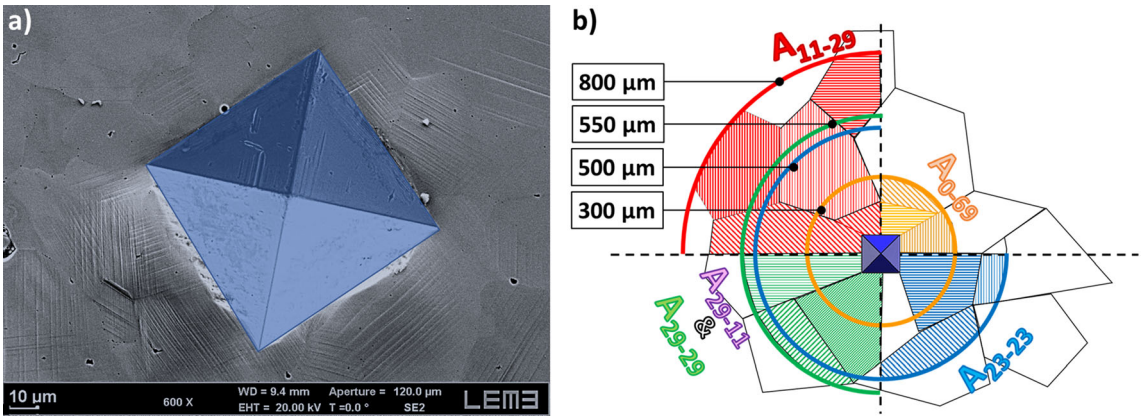

Fig. 7 Observation of the inelastic deformation induced during a hardness test: **a** on the edge of an imprint on alloy A_{11-29}, **b** cartographic representation of the zone affected by the phase transformation of the different alloys. The indentation is shown in blue (color figure online)

consisted of one single austenitic phase. Martensite was observed until a distance of 800 µm from the indentation center, i.e., 8 times the diagonal size of the indentation; it is 2.7 times larger than the A_{0-69} alloy. The multiphase alloys A_{23-23}, A_{29-11}, and A_{29-29} had an equivalent phase transformation affected zone, spreading until 500–550 µm far from the center of the indentation. The damping effect of the SMAs is intrinsically linked to the phase transformation. If the phase transformation spreads over a larger distance in the A_{11-29} alloy, its damping effect should be higher than that observed for the other HE-SMAs and the ternary alloy.

Thus, a good damping shape memory alloy is characterized by a large hysteresis (about 40 °C) and a high enthalpy (above 4 J g^{-1}) [57]. Figure 8 shows the thermograms of studied alloys (except for 1050A) over a range of − 60 to 300 °C. NiTi and CuAlNi alloys show a good reversible transformation. The ternary alloy A_{0-69} (FeMnV) shows a reversible phase transformation upon heating and cooling but with low enthalpy of 1 J g^{-1} (10 times less than the NiTi alloy). For A_{23-23} and A_{29-29} alloys in the ST state, the curve on cooling is flat while a high-intensity peak (5 J g^{-1} of the order of copper SMAs) is observed on heating. For A_{29-29} and A_{11-29} alloys in the ST state, no peak corresponding to the transformation could be distinguished on the thermograms during the heating or cooling stages. This absence of significant peaks by DSC is due to an absence or too low thermal martensitic transformation enthalpy for A_{29-11} and A_{11-29} alloys. These flat thermograms are in agreement with their diffractograms which show only austenitic phases. These flat thermograms are in agreement with their diffractograms

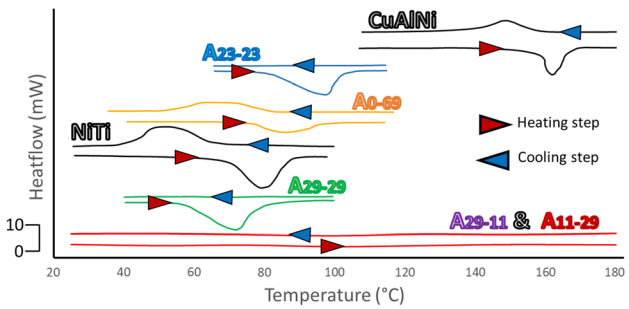

Fig. 8 Thermograms of studied alloys in the ST state

which show only austenitic phases. It should be noted that only the ternary CuAlNi alloy has a phase transformation that occurs above 100 °C.

Analysis of the Damping Capacity at Different Temperatures

Figure 9 shows the average height of the first ball bounce on each alloy at different temperatures. During the analysis of the stored images using the digital correlation camera, several types of damping responses occurred. The first one was observed for five alloys: NiTi, CuAlNi, A_{0-69}, A_{23-23}, and A_{29-29}. The damping behavior of these alloys drops drastically above the A_f transformation temperature: the rebound height was increasing with increasing temperature. This kind of response is the less interesting one for the study. The second kind of response was observed only for the 1050A alloy. The rebound height decreases when increasing the temperature of this alloy. However, the depth and diameter of the dent left after the first rebound

were increasing with temperature due to the high ductility of this nearly pure (or commercially pure) low entropy alloy. These results are in agreement with the literature [58, 59]. This behavior was not relevant to the current study too.

The third type was observed for the alloys A_{29-11} and A_{11-29}. The damping behavior of these two HEAs was evolving slightly but linearly with temperature. These results were in agreement with the thermograms of these two alloys which did not show any phase transformation related to temperature. Except for the 1050A alloy, the A_{11-29} alloy has the highest damping level over the four studied temperatures.

Figure 10 represents the evolution at room temperature of the average hardness, the average diameter of the dent and the average height of the first bounce for all the studied alloys.

For the 1050A alloy, one notices a correlation between the dent size and the hardness of the sample, which is related to the damping capacity. For instance, the 1050A alloy exhibits the largest dent diameter (360 µm) that corresponds to the smallest measured hardness (37 HV) (Fig. 10). Indeed, as shown in Fig. 9, whatever the temperature, this alloy exhibits the lowest bounce height characterizing hence a high damping capacity. In fact, the damping of a ductile sample occurs through the plasticity where the anelastic energy during the impact is partially dissipated whereas the subsequent part is stored through the irreversible plastic strain [51]. It is worth noticing that this correlation has not been clearly observed for the other seven studied alloys even if they had similar hardness and dent size (Fig. 10).

It is known that for an alloy, lower is the rebound height better is the damping capacity. However, for an SMA, it is suitable to also minimize the impact imprint to avoid other irreversible effects such as plasticity and/or TRIP effects that can modify the overall SMA behavior and may reduce its durability. Thus, the most interesting SMAs, in terms of damping capacity, are those combining a low rebound height with a reduced imprint size.

To this end, a performance indicator has been proposed to reflect an implicit relation between the value of HE-SMAs damping and the rebound height as well as the diameter of the impact imprints. This performance indicator facilitates the data-reduction of the experimental findings and comparison between the HE-SMA's damping capacity. It is expressed as the weighted sum of the normalized rebound height (λ_1) and dent diameter (λ_2). It reads as follows:

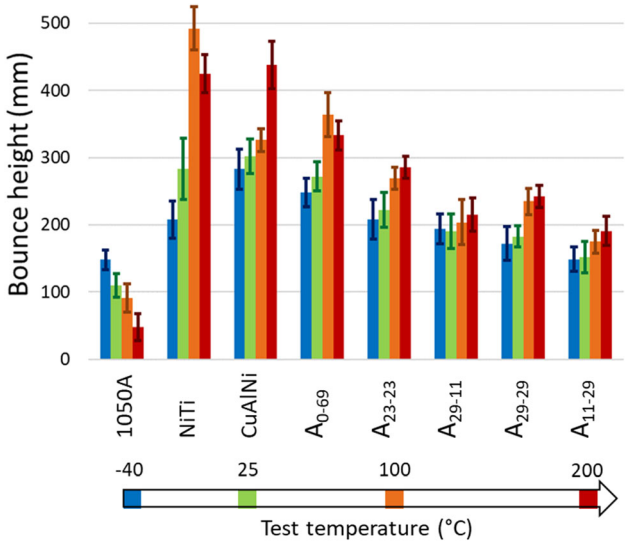

Fig. 9 Representation of the damping effect of the different alloys studied as a function of temperature. The bounce height is inversely proportional to the damping capacity of the alloys

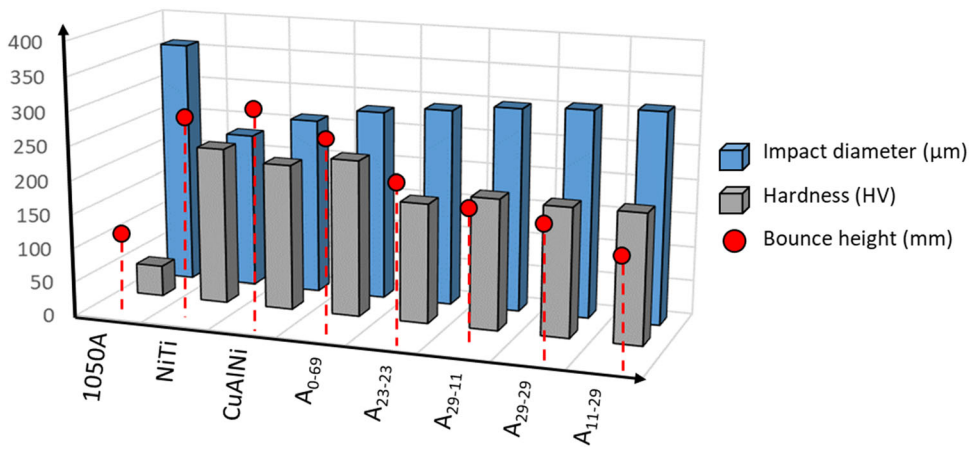

Fig. 10 Graphical representation of the three quantities for each of the studied alloys at *room temperature*: in red the average height of the ball rebound after impact (mm), in blue the average diameter of the imprint left by the impactor after impact (mm), in grey the average hardness (HV) in the *ST metallurgical state* (color figure online)

$$F = \alpha\lambda_1 + (1-\alpha)\lambda_2,$$

$$where \quad \lambda_1 = \frac{h_{max} - h}{h_{max} - h_{min}}$$

$$\lambda_2 = \frac{d_{max} - d}{d_{max} - d_{min}}$$

and α : ponderation factor.

As mentioned above, the most interesting SMAs, in terms of damping capacity, are thus characterized by a performance indicator close to 1.

Figure 11 represents the evolution of the performance indicator with respect to the operating temperature range (− 40 °C, 25 °C, 100 °C, 200 °C) for all the alloys. The performance indicator is computer considering an iso-weighting of the rebound height and the dent's imprint diameter. The ponderation factor is then set to a = 0.5.

It clearly shows the advantage of using the high entropy damping alloys notably A_{29-11} and A_{29-29} and specifically the HE-SMA, A_{11-29} over a wide temperature range. In fact, by considering a performance indicator ranging between [0.8–1], one can notice that the damping capacity of the A_{11-29} alloy is the most important and remains high for all the operating temperatures compared to the other tested alloys. This is the only alloy composed of the austenite observed first in this study, with a cell parameter of 0.352 nm. So this phase seems very promising for damping properties. In addition, as expected one can confirm that the NiTi alloy exhibits a very good damping capacity from − 40 to 25 °C but it loses its damping capacity at relatively high temperatures between 100 and 200 °C.

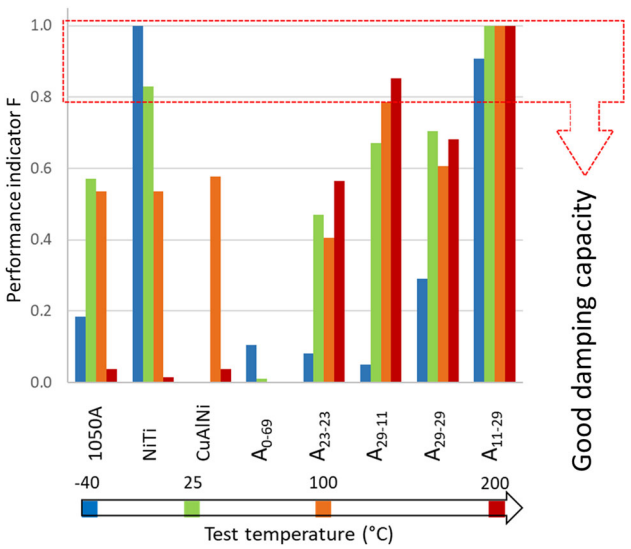

Fig. 11 Performance indicator representation of the different studied alloys for a wide range of operating temperatures

Effects of Aging on Damping Properties

This lack of explicit correlation between hardness and damping effect has been reported in beta-titanium alloys or SMAs [60, 61]. The loss of damping effect at room temperature or during thermal aging treatment has been also studied previously by Zhong et al. [31], Liu et al. [33] and Zhang et al. [62]. In the present study, an accelerated aging has been performed in an oven without a protective atmosphere (800 h at 250 °C) for all the alloys.

After one month of aging (800 h), a preliminary qualitative analysis has been performed. It has been noticed that some samples have altered their color due to the thermal oxidation visible to the naked eye. This was all the more visible on the CuAlNi alloy which showed a dark matte black oxide. The NiTi alloy turned into a golden-brown color. The A_{0-69} alloy turned blue after aging. For the other samples (1050A, A_{23-23}, A_{29-11}, A_{29-29}, and A_{11-29}), no color modification was observed.

A quantitative analysis was carried out using SEM observations realized on the aged samples. Both NiTi and A_{0-69} alloys were subject to precipitation at the grain boundaries, grain growth has occurred in the CuAlNi alloy as reported in the literature [63]. The variation of the damping properties of the alloys after the aging period with respect to those determined on the unaged alloys at room temperature is presented in Table 4.

The 1050A alloy presented a decreased hardness by 24% while the dent diameter was increased by the same proportion in comparison to the unaged state at room temperature. Thus, the aged sample was presenting a larger plastic zone whereas the rebound height decreased by 45%.

The NiTi alloy has developed precipitations during the aging [64, 65]. The precipitates have induced a hardening of the NiTi alloy (21% increase in hardness) but they also have limited the reversible martensitic phase transformation. The martensite was then retained after impact and the NiTi alloy behavior was similar to a ductile alloy, such as the 1050A where the damping capacity is induced by plasticity. This is confirmed by the 60% increase in dent size.

In the CuAlNi alloys, cracks located at the grain boundaries were visible after the impact: the weight drop test has entailed grain de-cohesion. Moreover, its hardness has increased by 30%. This increase was not compatible with grain growth as reported in [66, 67]. Precipitates have been observed by SEM analysis at the grain boundaries; this has induced brittleness and a cracks phenomenon in these areas [68].

The low entropy ternary alloy A_{0-69} has displayed a hardening by precipitation (40%) and the rebounds were 14% higher than those measured on unaged samples of this alloy. The average dent size was decreased by the same

Table 4 Property variations at room temperature after aging

Alloys	Property variations after aging (%)		
	Hardness	Bounce height	Impact diameter
1050A	**− 24.4**	**− 45.5**	25.0
NiTi	21.2	7.1	**60.9**
CuAlNi	33.0	20.0	7.7
$A_{0–69}$	**40.3**	14.8	**− 14.3**
$A_{23–23}$	25.0	**22.7**	− 3.4
$A_{29–11}$	9.4	5.3	− 1.7
$A_{29–29}$	11.1	11.1	1.6
$A_{11–29}$	8.1	3.3	0.3

Bold data indicates the alloys whose characteristics change the most after the aging heat treatment either in positive or negative for the 3 data studied.

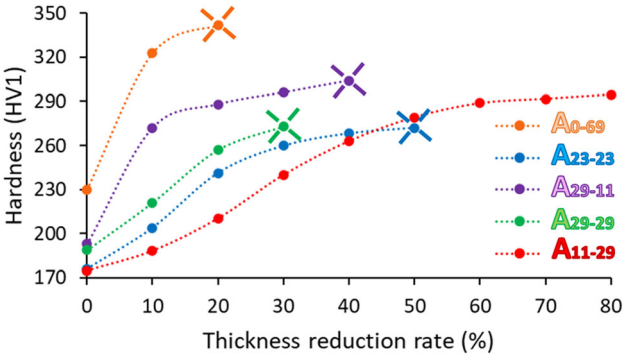

Fig. 12 Analysis of the ductility and the evolution of the hardness of the alloys during the cold rolling phases of $A_{0–69}$ to $A_{11–29}$ alloys in the ST state. The $A_{11–29}$ alloy exhibit a capacity for structural hardening as well as an important capacity for the cold forming process

amount. The damping capacities of $A_{23–23}$ (strongly dendritic) and $A_{29–29}$ (globular) alloys were decreased by the aging heat treatment. Indeed, the rebound heights, as well as the hardness of these two alloys, were higher than those of unaged samples and in the same proportions but their impact sizes were remaining comparable to the unaged configuration. $A_{29–11}$ (low dendritic) and $A_{11–29}$ (single-phase) alloys were the alloys whose damping capacities were less degraded by the aging heat treatment as shown in Table 4. Indeed, the evolution due to the aging was limited and did not exceed 9% for the hardness, 5% for rebound and almost no modification of the dent size. This confirms again that the new austenite phase is very stable over a large range of temperatures even for long-duration treatment.

Cold Workability

To be used in industrial applications, alloys must have good formability. Also, the cold formability of studied ST alloys $A_{0–69}$ to $A_{11–29}$ was carried out by cold rolling at room temperature using a jeweler's roller mill. Square cross-section samples ($7 \times 7 \times 6$ mm^3) were cut by machining from the ingots and rectified to have the same initial cross-section for each sample. Each rolling phase consisted of several successive steps where the sample was placed between the rollers of the rolling mill to reach a strain level of 10%. After each step, the hardness of the sample was measured. The sample was kept for the next steps if and only if no crack was observed. The formability analysis was stopped for a sample as soon as it was containing detectable cracks or when its thickness was equal to 1 mm, corresponding to a thickness reduction of 80%. The results are reported in Fig. 12; crosses indicate the appearance of cracks. The alloys show different ductility levels and cold working hardening abilities. The ternary $A_{0–69}$ alloy had the highest hardness, even higher than the CuAlNi and NiTi alloys; its formability was limited to a 20% reduction rate. It could be due to its martensitic structure. The quinary $A_{11–29}$ alloy, which is a single-phase alloy, had the highest ductility. It was the unique alloy that did not show crack, even at 80% reduction. As in previous studies, the ductility of some single-phase HEAs and HE-SMAs has been shown by Lohmuller et al. [69] and Peltier et al. [70] whose chemical compositions of alloys validate the five criteria related to high entropy in Table 2 (i.e., ΔS_{mix}, ΔH_{mix}, δ, EN and VEC).

Concluding Remarks

In this study, CuFeMnNiV-based HE-SMAs show excellent damping performance, with a damping value that represents two times that of nitinol in the case of the four studied operating temperatures ranging between [− 40 to 200 °C].

The successful development of new HEAs can be enhanced by the use of the following parameters: configurational entropy ΔS_{mix}, enthalpy of mixing ΔH_{mix}, atomic size difference δ, Pauling electronegativity and valence electron concentration VEC.

The use of the equivalence table allows the transposition of a ternary FeMnCr shape memory alloy into quinary high entropy shape memory alloys: the four manufactured HE SMAs have a martensitic phase transformation. The choice of replacing the Cr element with the V is confirmed by the relevant work of Utepov in 2008 [71], which shows that when Cr is substituted by V, these alloys display higher damping properties.

As reported in the literature, the best performing alloys in terms of damping are magnesium-based. This is particularly the case when the alloys contain iron and nickel.

The cocktail effect characterizing the HEAs allows the mixing of several elements of CuNiFeMnV leading hence to optimized damping capacity for the developed HE-SMAs. As in previous studies [70, 72], the sluggish diffusion due to the high entropy character of the alloys maintains the damping capacity of the HE-SMAs at high temperatures as well as during a long-term aging process.

The variation of the copper, nickel and iron content in the different alloys induced the evolution of the number and the nature of the phases observed in the obtained alloy. The two single-phase alloys (A_{0-69} and A_{11-29}) are those whose enthalpy of mixtures is negative but higher than − 10. The alloys with dendritic phases are the alloys whose mixing enthalpies are close to 0 (A_{23-23} and A_{29-11}). The multi-component alloy A_{29-29} has a score of mixing enthalpies of 3.64.

This study demonstrates that the chemical composition of alloys affects the ductility and suitability for structural hardening by cold forming. Zhang et al. [7] explain that these two characteristics are important in the choice of a damping alloy for industrial application. The austenitic A_{11-29} alloy shows a higher ductility, a better damping behavior and higher thermal stability between − 40 and 200 °C than the low entropy alloys FeMnV, NiTi, and CuAlNi.

Acknowledgements This research was supported by the SMART team of the laboratory LEM3. We thank warmly our colleagues Ethan Schaefer and Alae Eddine El Mikali who provided help that strongly assisted this study. Special thanks to Nimesis Technology for the supply of NiTi and CuAlNi alloys with damping behaviors.

References

1. Cantor B, Chang ITH, Knight P, Vincent AJB (2004) Microstructural development in equiatomic multicomponent alloys. Mater Sci Eng A 375–377:213–218. https://doi.org/10.1016/j.msea.2003.10.257
2. Zhou Y, Zhou D, Jin X et al (2018) Design of non-equiatomic medium-entropy alloys. Sci Rep 8:1–9. https://doi.org/10.1038/s41598-018-19449-0
3. Chen J, Zhou X, Wang W et al (2018) A review on fundamental of high entropy alloys with promising high–temperature properties. J Alloys Compd 760:15–30. https://doi.org/10.1016/j.jallcom.2018.05.067
4. Guo S, Liu CT (2011) Phase stability in high entropy alloys: formation of solid-solution phase or amorphous phase. Prog Nat Sci Mater Int 21:433–446. https://doi.org/10.1016/S1002-0071(12)60080-X
5. Ding Q, Zhang Y, Chen X et al (2019) Tuning element distribution, structure and properties by composition in high-entropy alloys. Nature 574:223–227. https://doi.org/10.1038/s41586-019-1617-1
6. Alaneme KK, Umar S (2018) Mechanical behaviour and damping properties of Ni modified Cu–Zn–Al shape memory alloys. J Sci Adv Mater Devices 3:371–379. https://doi.org/10.1016/j.jsamd.2018.05.002
7. Zhang Y, Zhu S (2008) Seismic response control of building structures with superelastic shape memory alloy wire dampers. J Eng Mech 134:240–251. https://doi.org/10.1061/(asce)0733-9399(2008)134:3(240)
8. Fukuhara M, Yin F, Ohsawa Y, Takamori S (2006) High-damping properties of Mn–Cu sintered alloys. Mater Sci Eng A 442:439–443. https://doi.org/10.1016/j.msea.2006.05.163
9. Zuo S, Xiao F, Fukuda T (2019) Orientation dependence of damping behavior in a Mn–Cu shape memory alloy. Scr Mater 170:95–98. https://doi.org/10.1016/j.scriptamat.2019.05.042
10. Jiang ZC, Tian QC, Ren ZM et al (2019) Development and characterization of a MnCu-based high damping alloy plate. IOP Conf Ser Mater Sci Eng. https://doi.org/10.1088/1757-899X/542/1/012020
11. Baik SH (2000) High damping Fe–Mn martensitic alloys for engineering applications. Nucl Eng Des 198:241–252. https://doi.org/10.1016/S0029-5493(99)00268-X
12. Jee KK, Jang WY, Baik SH et al (1997) Damping capacity in Fe–Mn based alloys. Scr Mater 37:943–948. https://doi.org/10.1016/S1359-6462(97)00198-X
13. Jee KK, Jang WY, Baik SH, Shin MC (1999) Damping mechanism and application of Fe–Mn based alloys. Mater Sci Eng A 273–275:538–542. https://doi.org/10.1016/s0921-5093(99)00395-0
14. Wang W, Chen Q, Liu R et al (2021) Synergistic damping effect mechanism of magneto-mechanical hysteresis and dislocations energy dissipation in FeMnCrCo high entropy alloys. Mater Sci Eng A 818:1–9. https://doi.org/10.1016/j.msea.2021.141412
15. Huang SK, Wen YH, Li N et al (2008) Application of damping mechanism model and stacking fault probability in Fe–Mn alloy. Mater Charact 59:681–687. https://doi.org/10.1016/j.matchar.2007.05.023
16. Girish BM, Satish BM, Mahesh K (2010) Effect of stacking fault probability and ε martensite on damping capacity of Fe-16%Mn alloy. Mater Des 31:2163–2166. https://doi.org/10.1016/j.matdes.2009.11.003
17. Adachi K, Wayman CM (1985) Transformation behavior of nearly stoichiometric Ni–Mn alloys. Metall Trans A 16:1567–1579. https://doi.org/10.1007/BF02663013
18. Ryazhkin AV, Babanov YA, Pilugin VP et al (2001) Determination of the local structure of the first and second shells in ordered and disordered Ni–Mn alloys. J Synchrotron Radiat 8:300–301. https://doi.org/10.1107/S090904950001894X
19. Wu SK, Lin HC (2003) D amping characteristics of TiNi binary and ternary shape memory alloys. J Alloys Compd 355:72–78
20. Chang SH, Liao BS, Gholami-Kermanshahi M (2020) Effect of Co additions on the damping properties of Cu–Al–Ni shape memory alloys. J Alloys Compd 847:156560. https://doi.org/10.1016/j.jallcom.2020.156560
21. Bertrand E, Castany P, Gloriant T (2013) Investigation of the martensitic transformation and the damping behavior of a superelastic Ti–Ta–Nb alloy. Acta Mater 61:511–518. https://doi.org/10.1016/j.actamat.2012.09.065
22. Achitei DC, Al Bakri Abdullah MM, Sandu AV et al (2014) On the fatigue of shape memory alloys. Key Eng Mater 594–595:133–139. https://doi.org/10.4028/www.scientific.net/KEM.594-595.133
23. Bujoreanu LG, Lohan NM, Pricop B, Cimpoeşu N (2012) On role of atomic migration in amnesia occurrence during complex thermal cycling of Cu–Zn–Al shape memory alloy. Mater Sci Technol (United Kingdom) 28:658–667. https://doi.org/10.1179/1743284711Y.0000000099

24. Wang YD, Ren Y, Li H et al (2006) Tracing memory in polycrystalline ferromagnetic shape-memory alloys. Adv Mater 18:2392–2396. https://doi.org/10.1002/adma.200600480
25. Piedboeuf MC, Gauvin R, Thomas M (1998) Damping behaviour of shape memory alloys: strain amplitude, frequency and temperature effects. J Sound Vib 214:885–901
26. He Y, Yin H, Zhou R, Sun Q (2010) Ambient effect on damping peak of NiTi shape memory alloy. Mater Lett 64:1483–1486. https://doi.org/10.1016/j.matlet.2010.03.068
27. Yin H, Yan Y, Huo Y, Sun Q (2013) Rate dependent damping of single crystal CuAlNi shape memory alloy. Mater Lett 109:287–290. https://doi.org/10.1016/j.matlet.2013.07.062
28. Toker GP, Saedi S, Acar E et al (2020) Loading frequency and temperature-dependent damping capacity of NiTiHfPd shape memory alloy. Mech Mater 150:103565. https://doi.org/10.1016/j.mechmat.2020.103565
29. Jensen, Schwaneke, Walsh (1962) Fatigue properties of manganese copper damping alloys
30. Yin FX, Iwasaki S, Sakaguchi T, Nagai K (2006) Susceptibility of damping behavior to the solidification condition in the as-cast M2052 high-damping alloy. Key Eng Mater 319:67–72. https://doi.org/10.4028/www.scientific.net/kem.319.67
31. Zhong Z, Liu W, Li N et al (2016) Mn segregation dependence of damping capacity of as-cast M2052 alloy. Mater Sci Eng A 660:97–101. https://doi.org/10.1016/j.msea.2016.02.084
32. Zhu R, Mao B, Zhao Q et al (2021) Dynamic characteristics of Mn–Cu high damping alloy subjected to impact load. Adv Mech Eng 13:1–20. https://doi.org/10.1177/16878140211013616
33. Liu W, Li N, Zhong Z et al (2016) Novel cast-aged MnCuNi-FeZnAl alloy with good damping capacity and high usage temperature toward engineering application. Mater Des 106:45–50. https://doi.org/10.1016/j.matdes.2016.05.098
34. Yin F, Takamori S, Ohsawa Y et al (2002) The effects of static strain on the damping capacity of high damping alloys. Mater Trans 43:466–469. https://doi.org/10.2320/matertrans.43.466
35. Ma SG, Liaw PK, Gao MC et al (2014) Damping behavior of Al_xCoCrFeNi high-entropy alloys by a dynamic mechanical analyzer. J Alloys Compd 604:331–339. https://doi.org/10.1016/j.jallcom.2014.03.050
36. Song R, Ye F, Yang C, Wu S (2018) Effect of alloying elements on microstructure, mechanical and damping properties of Cr–Mn–Fe–V–Cu high-entropy alloys. J Mater Sci Technol 34:2014–2021. https://doi.org/10.1016/j.jmst.2018.02.026
37. Chen K, Yan J, Li N et al (2020) The effect of the annealing temperature on the damping capacity under constant prestress, mechanical properties and microstructure of an Fe–11Cr–2.5Mo–0.1Zr–1.0Ni forged damping alloy. J Alloys Compd 815:152429. https://doi.org/10.1016/j.jallcom.2019.152429
38. Chen Q, Zhang H, Zhou S et al (2019) A novel high-entropy alloy with excellent damping property toward a large strain amplitude environment. J Alloys Compd 802:493–501. https://doi.org/10.1016/j.jallcom.2019.06.247
39. Lei Z, Wu Y, He J et al (2020) Snoek-type damping performance in strong and ductile high-entropy alloys. Sci Adv 6:1–9. https://doi.org/10.1126/sciadv.aba7802
40. Yasar E, Gungunes H, Akturk S, Durlu TN (2007) New observations on the formation of a thermal martensite in Fe–Ni–Mo alloys. J Alloys Compd 428:125–129. https://doi.org/10.1016/j.jallcom.2006.03.051
41. Tian Y, Borgenstam A, Hedström P (2018) Comparing the deformation-induced martensitic transformation with the athermal martensitic transformation in Fe–Cr–Ni alloys. J Alloys Compd 766:131–139. https://doi.org/10.1016/j.jallcom.2018.06.326
42. Güner M, Güler E, Yasar E, Aktas H (2007) Some aspects of thermally induced martensite in Fe-30% Ni-5% Cu alloy. Phys B Condens Matter 395:16–19. https://doi.org/10.1016/j.physb.2007.01.032
43. Hume-Rothery W (1966) Atomic diameters, atomic volumes and solid solubility relations in alloys. Acta Metall 14:17–20. https://doi.org/10.1016/0001-6160(66)90267-7
44. Yeh JW (2013) Alloy design strategies and future trends in high-entropy alloys. JOM 65:1759–1771. https://doi.org/10.1007/s11837-013-0761-6
45. Zhang Y, Zhou YJ, Lin JP et al (2008) Solid-solution phase formation rules for multi-component alloys. Adv Eng Mater 10:534–538. https://doi.org/10.1002/adem.200700240
46. Guo S, Ng C, Lu J, Liu CT (2011) Effect of valence electron concentration on stability of FCC or BCC phase in high entropy alloys. J Appl Phys. https://doi.org/10.1063/1.3587228
47. Clough RB, Webb SC, Armstrong RW (2003) Dynamic hardness measurements using a dropped ball: with application to 1018 steel. Mater Sci Eng A 360:396–407. https://doi.org/10.1016/S0921-5093(03)00499-4
48. Emminger C, Cakmak UD, Preuer R et al (2021) Hyperelastic material parameter determination and numerical study of TPU and PDMS dampers. Materials. https://doi.org/10.3390/ma14247639
49. Chung SW, Kwak JB (2020) A novel evaluation of shock absorption and adhesive strength under shear impact loading. J Adhes. https://doi.org/10.1080/00218464.2020.1804375
50. Stanford MK (2016) Hardness and microstructure of binary and ternary nitinol compounds. Nasa/Tm—2016-218946 46
51. Penchal Reddy M, Manakari V, Parande G et al (2018) Enhancing compressive, tensile, thermal and damping response of pure Al using BN nanoparticles. J Alloys Compd 762:398–408. https://doi.org/10.1016/j.jallcom.2018.05.205
52. ASTM F 2004 (2008) Standard test method for transformation temperature of nickel-titanium alloys by thermal analysis
53. Yağcı NK, İnaç H (2019) Structural and magnetic study of Fe-15, 83% Mn-2, 18%V and Fe-18, 50% Mn-2, 27% Cu alloys. Int J Eng Res Dev. https://doi.org/10.29137/umagd.414647
54. Jo YH, Choi WM, Kim DG et al (2019) FCC to BCC transformation-induced plasticity based on thermodynamic phase stability in novel $V_{10}Cr_{10}Fe_{45}Co_xNi_{35-x}$ medium-entropy alloys. Sci Rep. https://doi.org/10.1038/s41598-019-39570-y
55. Aydogdu A, Aydogdu Y, Adigüzel O (1997) Improvement of hardness and microstructures by ageing in shape memory CuAlNi alloys. J Phys IV. https://doi.org/10.1051/jp4:1997549
56. Cui Q, Ohori K (2000) Grain refinement of high purity aluminium by asymmetric rolling. Mater Sci Technol 16:1095–1101. https://doi.org/10.1179/026708300101507019
57. Hedayati Dezfuli F, Alam MS (2014) Performance-based assessment and design of FRP-based high damping rubber bearing incorporated with shape memory alloy wires. Eng Struct 61:166–183. https://doi.org/10.1016/j.engstruct.2014.01.008
58. Gruber B, Weißensteiner I, Kremmer T et al (2020) Mechanism of low temperature deformation in aluminium alloys. Mater Sci Eng A. https://doi.org/10.1016/j.msea.2020.139935
59. Yogo Y, Sawamura M, Harada R et al (2017) Stress–strain curve of pure aluminum in a super large strain range with strain rate and temperature dependency. Procedia Eng 207:161–166. https://doi.org/10.1016/j.proeng.2017.10.755
60. Niem T, Gonschorek S, Wöstmann B (2021) New method to differentiate surface damping behavior and stress absorption capacities of common CAD/CAM restorative materials. Dent Mater 37:e213–e230. https://doi.org/10.1016/j.dental.2020.12.012
61. Peng PW, Ou KL, Chao CY et al (2010) Research of microstructure and mechanical behavior on duplex ($\alpha + \beta$) Ti–4.8Al–2.5Mo–1.4V alloy. J Alloys Compd 490:661–666. https://doi.org/10.1016/j.jallcom.2009.10.133

62. Zhang Y, Li N, Yan JZ, Xie JW (2014) Effect of the precipitated second phase during aging on the damping capacity degradation behavior of M2052 alloy. Adv Mater Res 873:36–41. https://doi.org/10.4028/www.scientific.net/AMR.873.36
63. Montecinos S, Cuniberti A, Romero R, Stipcich M (2015) Grain size evolution in Cu-based shape memory alloys. J Mater Sci 50:3994–4002. https://doi.org/10.1007/s10853-015-8956-6
64. Gall K, Sehitoglu H, Chumlyakov YI, Kireeva IV (1999) Tension-compression asymmetry of the stress-strain response in aged single crystal and polycrystalline NiTi. Acta Mater 47:1203–1217. https://doi.org/10.1016/S1359-6454(98)00432-7
65. Wagner MFX, Dey SR, Gugel H et al (2010) Effect of low-temperature precipitation on the transformation characteristics of Ni-rich NiTi shape memory alloys during thermal cycling. Intermetallics 18:1172–1179. https://doi.org/10.1016/j.intermet.2010.02.048
66. Montecinos S, Cuniberti A (2014) Effects of grain size on plastic deformation in a β CuAlBe shape memory alloy. Mater Sci Eng A 600:176–180. https://doi.org/10.1016/j.msea.2014.02.028
67. Sampath V (2005) Studies on the effect of grain refinement and thermal processing on shape memory characteristics of Cu–Al–Ni alloys. Smart Mater Struct. https://doi.org/10.1088/0964-1726/14/5/013
68. Lee JS, Wayman CM (1986) Grain refinement of a Cu–Al–Ni shape memory alloy by Ti and Zr additions. Trans Jpn Inst Met 27:584–591. https://doi.org/10.2320/matertrans1960.27.584
69. Lohmuller P, Peltier L, Hazotte A et al (2018) Variations of the elastic properties of the CoCrFeMnNi high entropy alloy deformed by groove cold rolling. Materials (Basel). https://doi.org/10.3390/ma11081337
70. Peltier L, Berveiller S, Meraghni F et al (2021) Martensite transformation and superelasticity at high temperature of $(TiHfZr)_{74}(NbTa)_{26}$ high-entropy shape memory alloy. Shape Mem Superelast. https://doi.org/10.1007/s40830-021-00323-4
71. Utepov TE (2008) Damping steel alloyed with chromium and vanadium for noise-combatting technology. Metallurgist 52:265–270. https://doi.org/10.1007/s11015-008-9044-9
72. Peltier L, Lohmuller P, Meraghni F et al (2020) Investigation and composition characterization of a "NiTi-like" alloy combining high temperature shape memory and high entropy. Shape Mem Superelast. https://doi.org/10.1007/s40830-020-00290-2